Experimental and numerical response and failure of laterally impacted carbon/glass fibre-reinforced hybrid composite laminates

Bin Liu [a,b], Wei Wang [a,c], Leigh Sutherland[d]

[a] Key Laboratory of High Performance Ship Technology (Wuhan University of Technology), Ministry of Education, Wuhan 430063, China

[b] Green & Smart River-Sea-Going Ship, Cruise and Yacht Research Centre, Wuhan University of Technology, Wuhan 430063, China

[c] School of Naval Architecture, Ocean and Energy Power Engineering, Wuhan University of Technology, Wuhan 430063, China

[d] Centre for Marine Technology and Ocean Engineering (CENTEC), Instituto Superior Técnico, Universidade de Lisboa, Lisbon 1049-001, Portugal

Abstract

The paper presents low-velocity impact tests and finite element simulations of carbon/glass fibre-reinforced hybrid composite laminates struck by a pyramidal frustum impactor in order to examine crushing deformations and failure mechanisms. Three mass ratios between the carbon and glass fibre (1:2, 1:1 and 2:1) are considered to compare the influence of the fibre hybridisation on the impact resistance of these laminates. This investigation is an essential step in the design process when ship structural crashworthiness is considered. The experimental results are presented in terms of the force-displacement responses and permanent deformations. Aspects of particular relevance to the deformation and fracture behaviour of hybrid-composite structures subjected to accidental loads are discussed, especially fibre/matrix debonding and fibre damage. Glass fibre shows better impact resistance than carbon fibre, despite the higher modulus of the latter. A series of simulations performed by the LS-DYNA finite element solver are used to calibrate the material failure criteria based on the experimental data, and the sensitivity of the failure criteria to mesh sizes is investigated.

Keywords

Hybrid composite; Carbon fibre; Glass fibre; Low-velocity impact; Experiment; Numerical simulation.

1. Introduction

Fibre reinforced polymer (FRP) composite materials are widely used for hull structures of high-speed craft because of their advantages in terms of lightweight, mechanical properties, forming of double curvatures and corrosion resistance. However, the higher sailing speeds increase the risk and consequence of ship collisions and hence increasing attention has been paid to this aspect since the relevant mechanical properties of composites are often of concern, especially when compared to those of steel [1-6].

Glass fibre reinforced polymer (GFRP) composites are traditionally the most commonly used marine composite materials, but increasingly carbon fibre reinforced polymer (CFRP) composites are being introduced into the marine industry due to their high specific modulus and excellent design feasibility [7-9]. Although the elastic moduli of CFRP composites are higher than those of GFRP composites, the much higher production cost of CFRP materials makes the development of hybrid composites combining the advantage of both materials attractive.

The damage mechanism of composites laminates under impact loadings may be categorised as either ‘intralaminar’, such as fibre/matrix debonding, fibre fracture, matrix cracking or plasticity, or ‘interlaminar’ failure in which debonding at the interface between adjacent plies to give the so-called ‘delamination’ [10]. Among these, delamination is one of the most detrimental results on the stiffness and strength of fibre composite materials [11, 12].

Recently, a series of impact tests on carbon/glass hybrid composites (CGHC) have been conducted where it was concluded that the impact response of hybrid laminates can be enhanced by providing the glass fibre on the back surface, since the glass fibre has higher failure strain, hence delaying the fracture initiation and propagation on the back surface [13, 14]. It was seen that both ply sequence and angle were significant for all mechanical properties of these composites. In particular, fibre tensile strength has the largest contribution to the impact resistance of composites for bending controlled impact events. The fibre volume fraction controls the material properties, affecting the specific modulus, stiffness and strength of composites under low-velocity impact [15]. In CGHC, the onset of fracture is mainly induced by the fracture of carbon fibre, and the glass fibre

bridges the crack path or reduces the spread of damage [16]. Generally, the carbon fibre has higher elastic modulus and stiffness than the glass fibre, but the glass fibre shows better fracture toughness and impact resistance. Hybridizing the fibres in a composite laminate can achieve a better mechanical performance [17]. The impact resistance of composite laminates is affected by the mixing ratio, thickness, ply sequence and angle, and many other material parameters [1-4].

Finite element simulation can be a cost-effective method to investigate the impact performance of composite materials. Many failure criteria for FRP composites have been proposed, and in the early material constitutive models it is assumed that the material is linear elastic before failure and the failure occurs immediately after satisfying the failure criterion [18]. The failure criteria of composite materials have been investigated for five decades; however, there is still not a unified criterion to predict successfully the failure behaviour of composite materials. Some classical failure criteria were proposed, such as Tsai-Wu, Hashin, Chang-Chang and Puck failure criterion [19-22]. These failure criteria have been widely applied with some success, but their limits of applicability are clearly defined [23]. In fact, damage progresses and evolves in the complex micro architecture of a composite material and the material properties are correspondingly gradually degraded until failure occurs. Moreover, a material failure criterion that is suitable for use with the coarsely meshed shell models commonly used in the ship collision analysis is required [24, 25].

Over the last two decades, various failure criteria were developed based on the assumptions of specific failure modes and mechanisms. Cuntze [26] presented a methodology based on the failure mode concept for the prediction of failure in composite laminates and good agreement was obtained between experimental and numerical results for laminates where fibre failure was the dominant mode. Later, LaRC (Langley Research Centre) series failure criteria based on the Hashin and Puck failure criterion were developed considering nonlinear matrix shear behaviour for laminated fibre-reinforced composites [27-30]. Correlation between experimental and numerical results was seen to be very satisfactory for the laminates suffering compressive failure. Li et al. [31] proposed a failure criterion considering the interaction between matrix-dominated and fibre-

dominated failure modes for fibre-reinforced composite materials under three-dimensional stress states. The proposed failure criterion was verified by a series of experiments for different kinds of unidirectional composites under various stress states.

Recently, Rezasefat et al. [32] compared the Cuntze and Puck failure criteria, employing them as inter-fibre failure criteria in combination with non-linear shear behaviour and damage evolution. Both failure criteria were able to predict approximately the same shape and area for the matrix damage caused by low-velocity impact. The failure model of Cuntze is preferable to that of Puck in the sense that a search algorithm is not required for the fracture angle, and hence the former explicit simulation becomes more efficient.

The present paper investigates the impact characteristics and failure of CGHC laminates subjected to a pyramidal frustum (truncated, flat ended, pyramid) impactor. This is achieved via low-velocity impact tests and finite element simulations. As pyramid type impactors are far more relevant to common impact scenarios in a marine environment than the hemispherical ones developed for the aeronautical fields [2, 33, 34], a pyramid shaped impactor is used in this paper. Further, to avoid unrepresentative very high initial contact pressures at the pointed tip of a true pyramid, a frustum (truncated pyramid) shape is utilised. The experimental results are analysed in terms of the force-displacement response and the failure mode of each specimen. A series of simulations performed by the LS-DYNA finite element solver are carried out to calibrate the failure criteria of the composite materials considered based on the experimental data. Moreover, the accuracy of the material failure criteria using various mesh sizes is investigated based on the simulations of experiments. The deformation and failure characteristics investigated in the present work are of considerable practical importance to assess the safety of the composite ship structures subjected to accidental loads.

2. Experimental setups

The experimental programme evaluates the impact response and failure of CGHC laminates struck by a mass with a pyramidal frustum impactor. Impacted plate dimensions are 560 × 400 × 3.0 mm

(Fig. 1). Laminates are fully clamped by twenty M16 bolts (which pass through holes in the clamped areas of the plates) between two thick rectangular steel plates (upper and lower support plates) with an internal cut-out of 400 × 240 mm. The upper and lower support plates are fixed to a strong structural 'anvil' base. This experimental setup has been used to realise a near-perfectly fully clamped plate condition in low-velocity impact tests [35, 36].

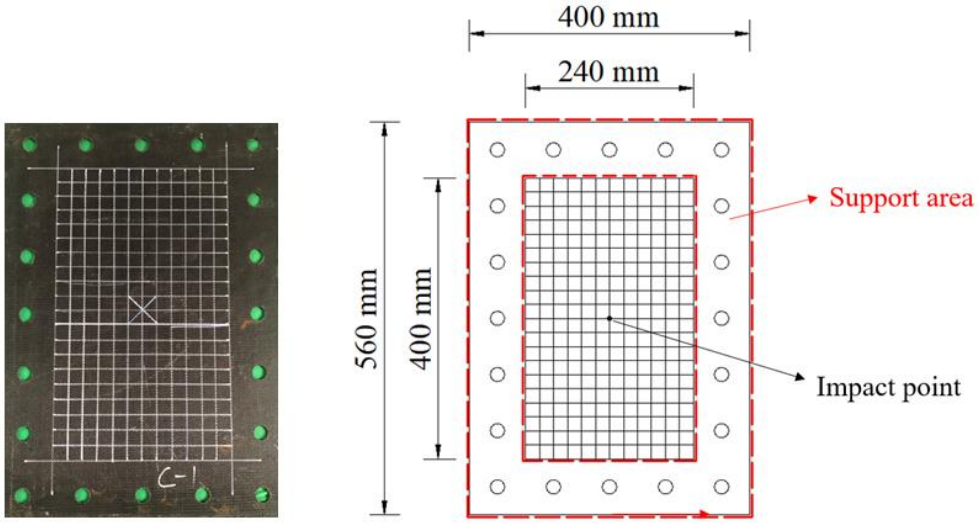

Fig. 1: Specimen dimensions.

Eight specimens were fabricated using various combinations of two distinct orthogonally woven plies, one of T300 carbon fibres and one of SW220 glass fibres. Vacuum bagging was utilized to manufacture the specimens, and the material properties of the plies made using these two fibres, provided by the manufacturer, are given in Table 1.

The glass-carbon fibre ply combinations in each of the test specimens are presented in Table 2. Specimen name notation consists of the material components ('C' for Carbon and 'G' for Glass), the mass ratio of these two components, and the initial impact velocity (V). For example, C1G1-V1.0 corresponds to a 1:1 carbon/glass hybrid composite laminate struck by an impactor with an initial impact velocity of 1.0 m/s. The three mass ratios between carbon and glass fibre (1:2, 1:1 and 2:1) were selected in order to compare the influence of the fibre hybridisation on the impact resistance of laminates. In addition, PC and PG correspond to the composite laminates fabricated using only carbon and glass fibres, respectively (as shown in Fig. 2).

Table 1: Material mechanical properties of carbon fibre and glass fibre composites.

Property	**Units**	**Carbon fibre**	**Glass fibre**
Density	kg/m^3	1600	1800
Percentage of breaking elongation	%	1.51	2.86
Young's modulus (E_{11})	GPa	35.0	12.0
Young's modulus (E_{22})	GPa	35.0	12.0
Young's modulus (E_{33})	GPa	10.3	6.0
Shear modulus (G_{12})	GPa	7.17	6.75
Shear modulus (G_{13})	GPa	3.78	3.0
Shear modulus (G_{23})	GPa	3.78	3.0
Poisson's ratio ($\nu_{12}=\nu_{21}$)	--	0.28	0.29
Longitudinal tensile strength (X_t)	MPa	470	700
Longitudinal compressive strength (X_c)	MPa	320	600
Transverse tensile strength (Y_t)	MPa	470	700
Transverse compressive strength (Y_c)	MPa	320	600
Shear strength (S)	MPa	109	20
Strain at longitudinal compressive strength (E_{11c})	--	0.0099	0.0099
Strain at longitudinal tensile strength (E_{11t})	--	0.027	0.027
Strain at transverse compressive strength (E_{22c})	--	0.0099	0.0099
Strain at transverse tensile strength (E_{22t})	--	0.027	0.027
Strain at shear strength (G_{ms})	--	0.028	0.028

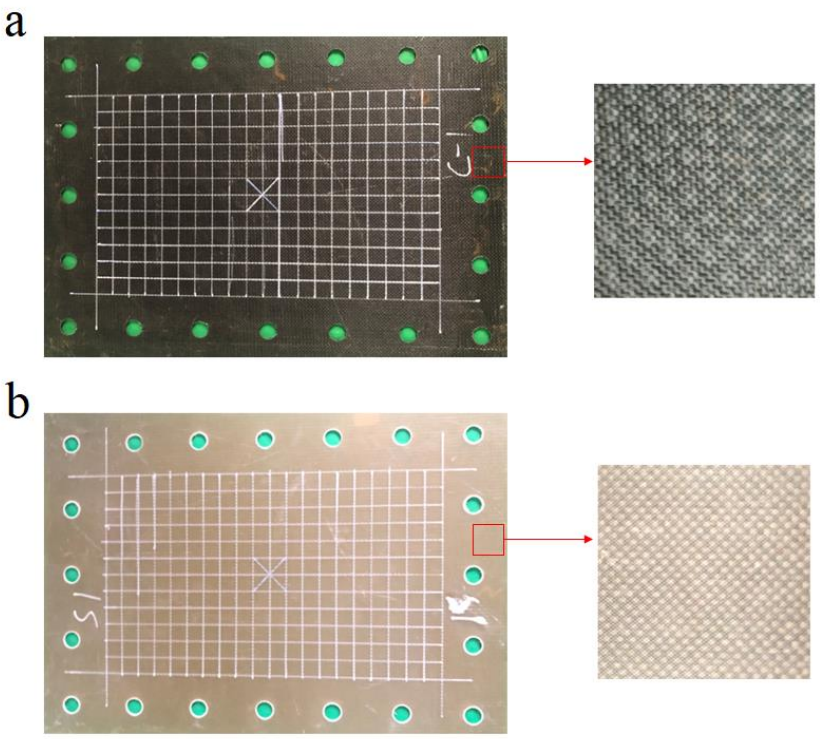

Fig. 2: Details of the (a) CFRP and (b) GFRP laminates.

Hybrid laminates contained alternate carbon and glass plies, and specimen ply thicknesses, sequences and angles are given in Table 2. As the reinforcement fibres are all of woven form, the ply angles 0° and 45° in Table 2 actually refer to 0° / 90° and ±45°, respectively. Outer plies were

kept as carbon fibre, with alternating glass and carbon plies between them to give the required fibre material mass ratio.

Table 2: Configurations for CGHC laminates.

Number	Specimen*	Configuration**
1	PC-V1.1	$0_C/45_C/0_C/45_C/0_C/45_C/0_C/45_C/0_C/45_C/0_C/45_C/0_C$
2	PG-V1.2	$0_G/45_G/0_G/45_G/0_G/45_G/0_G/45_G/0_G/45_G/0_G/45_G/0_G$
3	C1G1-V1.0	$0_C/45_G/0_C/45_G/0_C/45_G/0_C/45_G/0_C/45_G/0_C/45_G/0_C$
4	C1G1-V1.4	$0_C/45_G/0_C/45_G/0_C/45_G/0_C/45_G/0_C/45_G/0_C/45_G/0_C$
5	C1G2-V1.0	$0_C/45_G/0_G/45_C/0_G/45_G/0_C45_G/0_G/45_C/0_G/45_G/0_C$
6	C1G2-V1.3	$0_C/45_G/0_G/45_C/0_G/45_G/0_C45_G/0_G/45_C/0_G/45_G/0_C$
7	C2G1-V1.0	$0_C/45_C/0_G/45_C/0_C/45_G/0_C/45_C/0_G/45_C/0_C/45_G/0_C$
8	C2G1-V1.2	$0_C/45_C/0_G/45_C/0_C/45_G/0_C/45_C/0_G/45_C/0_C/45_G/0_C$

* C: carbon fibre; G: glass fibre; V: impact velocity.
** Ply thickness: 0.23mm.

The impact tests are conducted using a horizontal impact facility, as shown in Fig. 3. A wheeled trolley carrying a rigid impactor falls down an inclined slope before travelling along horizontal rails and striking the centre of the specimen. The impactor is fabricated with a pyramidal frustum nose with a 10 × 10 mm square flat end (Fig. 3) which is the contact area with the impacted specimens.

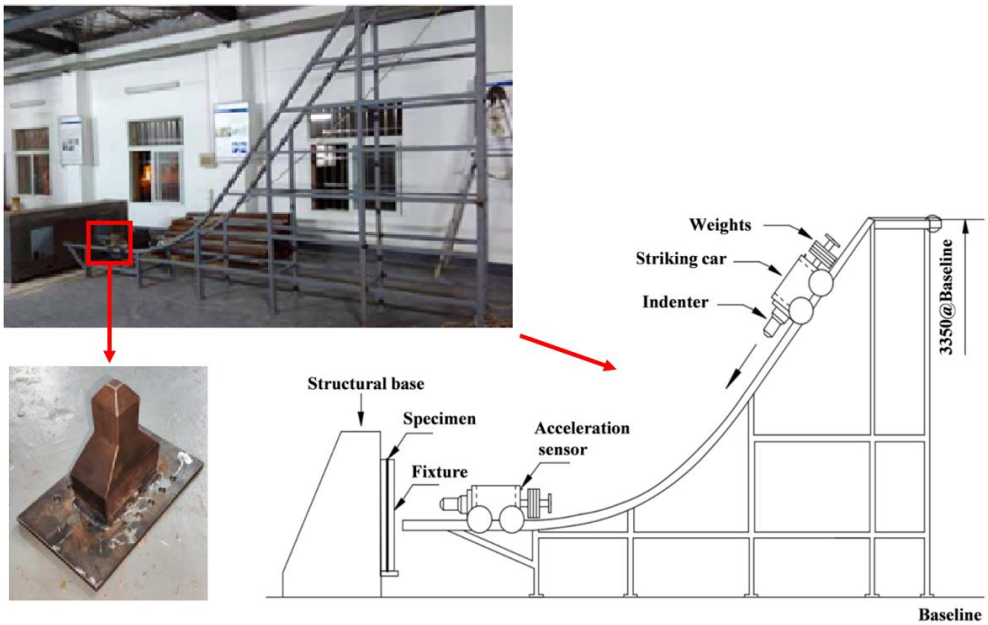

Fig. 3: Sketch of the horizontal impact facility.

The total mass of carriage and impactor is 100 kg. An acceleration sensor on the impactor gives the variation of the acceleration with time during the impact and an optical gate gives the incident velocity of the impactor. The histories of the impact force are calculated from the measured

acceleration-time data together with the mass of the impactor assembly. Velocity, displacement and absorbed energy are calculated from the force-time data by successive numerical integrations.

3. Experimental results

The experimental values of the deflection and absorbed energy corresponding to the peak force are summarised in Table 3, together with deflection and absorbed energy at the end of the impact event. This final energy value is that irreversibly absorbed by the specimen after any elastic energy releases due to rebound impactor. For perforated specimens the peak force indicates the onset of rupture, whereas for un-perforated specimens peak force represents the beginning of the rebound.

Table 3: Summary of experimental results.

Specimen	Input Energy (J)	Values at Peak Force			Values at End		Remarks
		Force (kN)	Defln (mm)	Energy (J)	Defln (mm)	Energy (J)	
PC-V1.1	60.5	8.1	13.0	43.0	15.4	56.8	Fracture
PG-V1.2	72	11.2	19.6	70.7	8.4	26.5	Deformation
C1G1-V1.0	50	9.9	13.6	50	3.2	18.8	Deformation
C1G1-V1.4	98	11.4	16.8	75.0	18.2	83.4	Fracture
C1G2-V1.0	50	9.7	15.2	49.5	1.7	16.7	Deformation
C1G2-V1.3	84.5	10.9	17.9	70.6	19.7	83.6	Fracture
C2G1-V1.0	50	11.4	13.9	50	5.0	20.5	Deformation
C2G1-V1.2	72	12.5	16.4	61.1	17.5	68.0	Fracture

The impact behaviour of the specimens is well described by the force-displacement curve (Fig. 4), making it suitable experimental data to compare with the numerical results. The slope of these curves represents the instantaneous stiffness of the specimen. Moreover, this plot indicates the ability of the specimens to resist impact loads and gives a measurement of the resistance of the specimen to the deformation before perforation. The experimental force-displacement curves show oscillations during the impact process, mainly caused by vibration of the rear plate of the impact vehicle on which the acceleration sensor is installed (Fig. 3).

The fracture morphologies of front and back surfaces of each composite laminate are shown in Fig. 5, to identify the impact damage modes.

3.1. Specimens PC-V1.1 and PG-V1.2

Comparing the force-displacement curve of the pure carbon specimen PC-V1.1 with that of the pure glass specimen PG-V1.2 (Fig. 4a), the slope of PC-V1.1 is seen to be higher than that of PG-V1.2

due to the higher stiffness of carbon fibre. However, specimen PC-V1.1 is already penetrated with an impact velocity of 1.1 m/s, whereas specimen PG-V1.2 still gives a rebound with an impact velocity of 1.2 m/s. This illustrates that here the carbon fibre plate is more easily fractured than the equivalent (in terms of thickness) glass fibre plate so that the GFRP plate, i.e. the latter has more impact resistance.

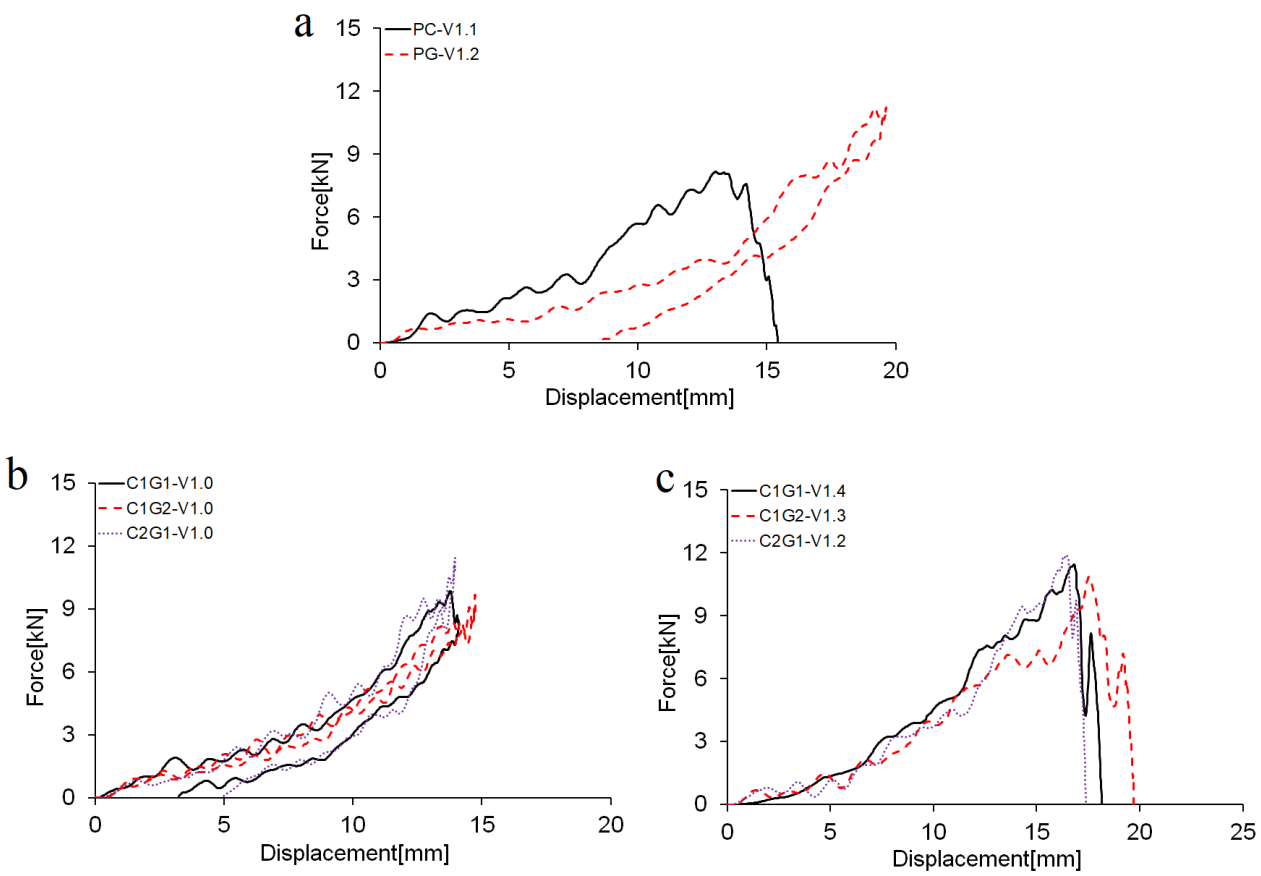

Fig. 4: Experimental force-displacement curves.

In Fig. 5(a), it is observed that a small square damage occurs at the front surface of the pure carbon specimen, while the back surface is completely split with significant matrix cracking and fibre breakage. The fibres are broken underneath the impactor in a brittle fracture mode. An obvious cruciform crack occurs at the back surface with a long crack (15 mm) aligned with the shorter span of specimen and a short crack (10 mm) aligned with the longer span.

In Fig. 5(b), corresponding to the pure glass specimen, only cracks are observed at the front surface contacted with the impactor edges. Some visible matrix cracks are observed at the back

surface and delamination occurs around the impact point. The relatively low stiffness of the glass fibres means that elastic deformation could absorb considerable impact energy before failure. Further, delamination then occurred to absorb more of the incident energy.

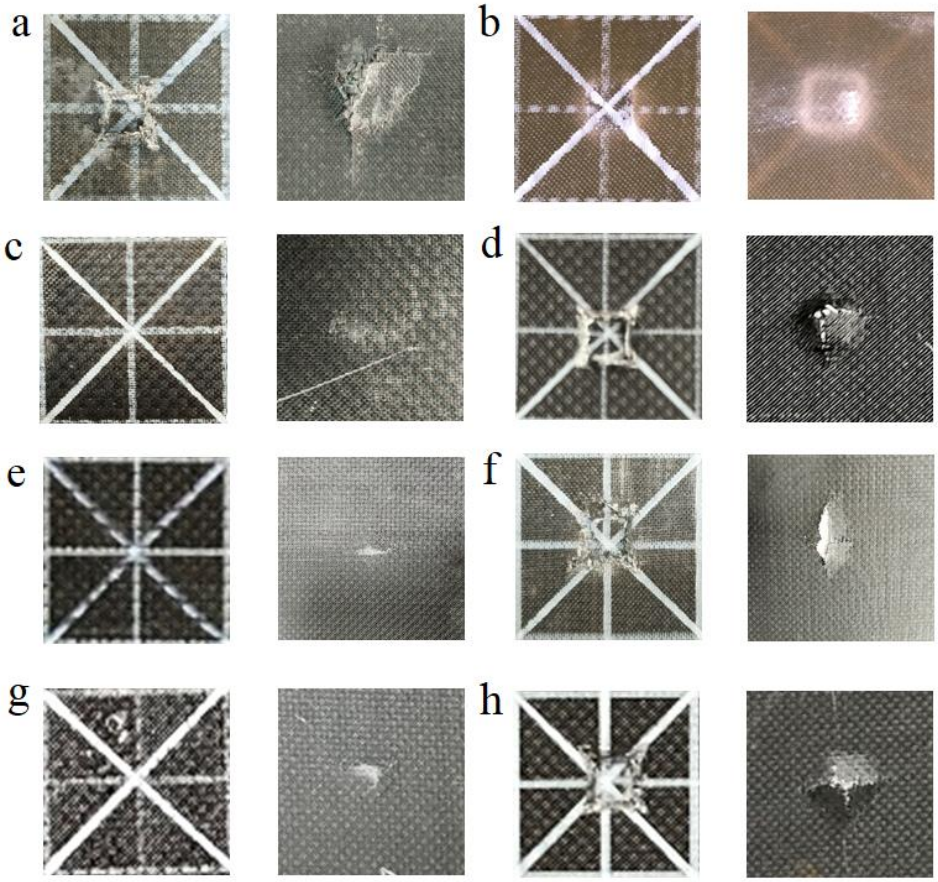

Fig. 5: Experimental failure patterns at the front and back surfaces of (a) PC-V1.1, (b) PG-V1.2, (c) C1G1-V1.0, (d) C1G1-V1.4, (e) C1G2-V1.0, (f) C1G2-V1.3, (g) C2G1-V1.0, (h) C2G1-V1.2.

3.2. Hybrid specimens (C1G1-V1.0, C1G2-V1.0 and C2G1-V1.0), lower impact velocity

Fig. 4(b) shows that all hybrid plates give a rebound under the impacts at the lower velocity of 1.0 m/s. The areas under the force-displacement curves indicate that approximately 35% of the incident energy is irreversibly absorbed by the laminates. A higher slope of the force-displacement curve is observed in the composite laminates with a higher proportion of carbon fibre content, since the carbon fibre has both higher tensile and shear moduli than does the glass fibre. Similarly, a higher carbon content leads to a higher peak force for the same impact energy. On the other hand, the higher elongation of the less stiff glass fibre gives the larger deformations seen for the composite laminates with a higher glass fibre content.

No laminate suffers serious damage (see Figs. 5c, e, g), with no significant damage at the front surface and only small matrix cracks and fibre debonding observed at the back surface.

3.3. Hybrid specimens (C1G1-V1.4, C1G2-V1.3 and C2G1-V1.2), higher impact velocities

The specimen carbon to glass ratio strongly affects the impact response here as seen in Fig. 4(c). Compared with the pure carbon specimen PC-V1.1, the energy absorption to fracture of specimens C2G1-V1.2, C1G1-V1.4 and C1G2-V1.3 are improved by approximately 20%, 46% and 47%, respectively. This illustrates that the impact resistance of carbon composite laminates can be improved by adding glass fibres, also indicating that there is a hybridisation ratio, above which further addition of glass is not as beneficial. This correlates with the hybrid effect first proposed by Marom et al. [37]. Some carbon fibres appear to fracture in tension, and then these broken carbon fibres together with the intact but lower stiffness glass fibres to which they are still bonded to continue to carry the loading. Further, the glass fibres may continue to transfer the load to the carbon fibre plies, preventing the immediate failure of the carbon fibre due to the high elongations seen. The higher elongation of the glass fibres also helps to give an effective stress release around the carbon fibres, enabling the material to exhibit a higher resistance to impact.

In Fig. 4(c), the peak force indicates the initial fibre damage in the composite laminates. After the peak force, a sudden drop is observed in the force-displacement curves, indicating the onset of severe fibre damage. Thus, the peak force and maximum displacement no longer occur at the same point in the force-displacement curve.

In the fractured specimens (Figs. 5d, f, h), a square damage of the same shape as the impactor is observed on the front surface of each specimen. On the back surface both carbon fibres and glass fibres are broken in clusters, along with debonding and fibre pull-out. Compared to the pure carbon specimen PC-V1.1 (Fig. 5a), these specimens suffer less damage even though the impact energies of the latter are greater. This almost certainly because the lower stiffness glass fibres appear to undergo a larger elastic deformation delaying the crack initiation and propagation.

4. Numerical model

Computations were performed using the explicit finite element package LS-DYNA, version 971 [38]. The finite element model of the impact event here is created in terms of three components: the composite laminate specimen, the upper and lower support plates and a representation of the impactor (see Fig. 6).

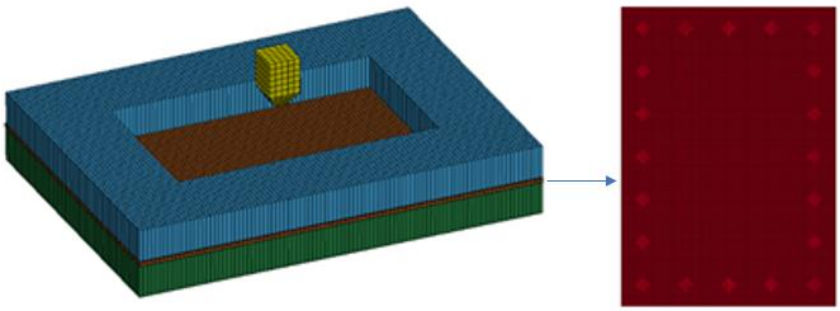

Fig. 6: Details of finite element model.

4.1. Support and impactor definition

The load capacity of a structure is strongly dependent on the restraints at the supports. When developing numerical models that are to be compared with experimental results, it is necessary to represent the actual boundary conditions instead of the ideal theoretical ones, since the assumptions of simply supported or fully clamped boundary conditions can produce errors in the load carrying capacity of the analysed structure [39, 40].

The present boundary conditions include the representation of the experimental supports, i.e. the upper and lower support plates interacting with the specimen (see Fig. 1). The specimen is clamped by the support plates, and no gap exists between the supports and the specimen plate. The upper and lower support plate is constrained in all degrees of freedom. As twenty bolts which pass through the specimen itself it is reasonable to assume that the longitudinal and transversal displacements of the clamped areas of the specimens in the experiments were negligible. Hence, nodal axial restrictions were imposed where the bolts pass through the plate in the numerical models. The contact between the supported portion of the plate and the supports was defined as

"Automatic Surface to Surface" with the friction coefficient of 0.2 [35]. The support plates were modelled by four-node shell elements and the mesh size was selected at 10 × 10 mm. The "Mat.020 - Rigid" was selected to ensure no deformation, assigning the mechanical properties and material density of the mild steel of which these plates were made in reality.

For the striking impactor, only the vertical translation was free, in whose direction the initial impact velocity was assigned. It should be mentioned that the vertical translation in the FEA model corresponded to the direction of movement of impactor in the horizontal impact facility (Fig. 3). The same LS-DYNA automatic contact was used between the striking mass and the specimen with the friction coefficient of 0.3 [35]. The experimental test impactor nose geometry was modelled accurately using solid elements, but to simplify the analysis the mass of the impactor / carriage and was modelled by only considering the impactor geometry with impactor a suitably increased density to achieve the mass as impactor plus carriage as used in the experiments. The steel striker was modelled using the same rigid material properties as was the support plates.

4.2. Definition of specimen plate

The specimen was modelled by four-node shell elements using the mesh size of 4.0 × 4.0 mm, which is in the order of plate thickness (3.0 mm) and is hence fine enough to capture the dynamic impact response. The Belytschko-Tsay shell element formulation was defined, since this formulation is the most economical and should be used when the membrane, bending and shear deformation are considered in the shell elements [38]. The chosen element is the conventional shell, which is suitable to the modelling of the thin-walled structures subjected to impact.

The ply thickness, sequence and angle of the composite laminates can be defined through the LS-DYNA parameter "Part Composite", and this was done to give the various with the experimental specimen lay-up configurations in the experiments (Table 2). The material properties of the composite laminates are the key definitions in an impact simulation. The material properties of carbon fibre and glass fibre composites given in Table 1 were used to define the material model. As the carbon and / or glass fibres are orthogonally woven and balanced in the plies, the modulus,

Poisson's ratio and strength were assumed equal in both transverse and longitudinal directions. In the present study, the selected material models are "MAT. 054/055 - Enhanced Composite Damage" and "MAT. 058 - Laminated Composite Fabric", where the (widely applied to analyse impact on composites) Chang-Chang, Tsai-Wu and Hashin failure criteria can be defined [38].

4.2.1. Chang-Chang failure criterion

The Chang-Chang failure criterion may be defined using the material model "MAT. 054/055 - Enhanced Composite Damage". For this criterion, four failure modes are described as follows:

(1) Tensile fibre mode, $\sigma_{aa} > 0$

$$e_f^2 = \left(\frac{\sigma_{aa}}{X_t}\right)^2 + \beta\left(\frac{\sigma_{ab}}{S}\right)^2 - 1 \rightarrow \begin{cases} e_f^2 \geq 0 \rightarrow \text{failure} \\ e_f^2 \leq 0 \rightarrow \text{elastic} \end{cases} \quad (1)$$

(2) Compressive fibre mode, $\sigma_{aa} < 0$

$$e_c^2 = \left(\frac{\sigma_{aa}}{X_c}\right)^2 - 1 \rightarrow \begin{cases} e_c^2 \geq 0 \rightarrow \text{failure} \\ e_c^2 \leq 0 \rightarrow \text{elastic} \end{cases} \quad (2)$$

(3) Tensile matrix mode, $\sigma_{bb} > 0$

$$e_m^2 = \left(\frac{\sigma_{bb}}{Y_t}\right)^2 + \left(\frac{\sigma_{ab}}{S}\right)^2 - 1 \rightarrow \begin{cases} e_m^2 \geq 0 \rightarrow \text{failure} \\ e_m^2 \leq 0 \rightarrow \text{elastic} \end{cases} \quad (3)$$

(4) Compressive matrix mode, $\sigma_{bb} < 0$

$$e_d^2 = \left(\frac{\sigma_{bb}}{2S}\right)^2 + \left[\left(\frac{Y_c}{2S}\right)^2 - 1\right]\frac{\sigma_{bb}}{Y_c} + \left(\frac{\sigma_{ab}}{S}\right)^2 - 1 \rightarrow \begin{cases} e_d^2 \geq 0 \rightarrow \text{failure} \\ e_d^2 \leq 0 \rightarrow \text{elastic} \end{cases} \quad (4)$$

where, subscript *a* and *b* refer to longitudinal and transverse directions, respectively; σ_{aa} and σ_{bb} are the nominal stresses in the composite laminate in the longitudinal and transverse directions, respectively; σ_{ab} is the nominal shear stress; X_t and X_c are the tensile and compressive strengths in the longitudinal direction, respectively; Y_t and Y_c are the tensile and compressive strengths in the transverse direction, respectively; S is the shear strength; β is the shear stress correction parameter in the tensile failure mode. Here, the value of β was considered as zero in the finite element analysis, since the maximum stress criterion shows better accuracy in the tensile fibre failure mode [38].

4.2.2. Tsai-Wu failure criterion

The Tsai-Wu failure criterion may also be defined using the material model "MAT. 054/055 - Enhanced Composite Damage". In this criterion, the same tensile and compressive fibre failure modes are used as for the Chang-Chang criterion (Eqs. 1 and 2). However, the definition of tensile and compressive matrix failure modes is different, and both are expressed by:

$$e_{md}^2 = \frac{\sigma_{bb}^2}{Y_c Y_t} + \left(\frac{\sigma_{ab}}{S}\right)^2 + \frac{\left(Y_c - Y_t\right)\sigma_{bb}}{Y_c Y_t} - 1 \rightarrow \begin{cases} e_{md}^2 \geq 0 \rightarrow \text{failure} \\ e_{md}^2 \leq 0 \rightarrow \text{elastic} \end{cases} \quad (5)$$

4.2.3. Hashin failure criterion

The Hashin failure criterion may be defined using the material model "MAT. 058 - Laminated Composite Fabric". This is an elastic damage model that is capable of modelling the damage independently in the principal directions of the materials. The model is based on the continuum damage mechanics approach and is formulated for plane stress conditions. In this criterion, four failure modes are considered:

(1) Tensile fibre mode, $\sigma_{aa} > 0$

$$e_f^2 = \left(\frac{\sigma_{aa}}{X_t}\right)^2 - 1 \rightarrow \begin{cases} e_f^2 \geq 0 \rightarrow \text{failure} \\ e_f^2 \leq 0 \rightarrow \text{elastic} \end{cases} \quad (6)$$

(2) Compressive fibre mode, $\sigma_{aa} < 0$

$$e_c^2 = \left(\frac{\sigma_{aa}}{X_c}\right)^2 - 1 \rightarrow \begin{cases} e_c^2 \geq 0 \rightarrow \text{failure} \\ e_c^2 \leq 0 \rightarrow \text{elastic} \end{cases} \quad (7)$$

(3) Tensile matrix mode, $\sigma_{bb} > 0$

$$e_m^2 = \left(\frac{\sigma_{bb}}{Y_t}\right)^2 + \left(\frac{\sigma_{ab}}{S}\right)^2 - 1 \rightarrow \begin{cases} e_m^2 \geq 0 \rightarrow \text{failure} \\ e_m^2 \leq 0 \rightarrow \text{elastic} \end{cases} \quad (8)$$

(4) Compressive matrix mode, $\sigma_{bb} < 0$

$$e_d^2 = \left(\frac{\sigma_{bb}}{2S}\right)^2 + \left(\frac{\sigma_{ab}}{S}\right)^2 - 1 \rightarrow \begin{cases} e_d^2 \geq 0 \rightarrow \text{failure} \\ e_d^2 \leq 0 \rightarrow \text{elastic} \end{cases} \quad (9)$$

4.2.4. Stiffness degradation

It must be noted that, after the composite plate suffers the internal damage under low-velocity impact, it does not directly lose all of its load bearing capacity; its performance gradually decreases until it fails completely. In addition to material failure, another important factor affecting the accuracy of simulations is the treatment of structural stiffness degradation.

The material stiffness degradation scheme is adopted by both Chang-Chang and Tsai-Wu failure criteria. The corresponding material elastic constant is degraded to zero according to different failure modes when the finite element fails (Table 4). The material constants E_{11}, E_{22}, G_{12}, v_{12} and v_{21} are set to zero in the corresponding unidirectional layer of the composite shell element in tensile fibre failure mode. In the compressive fibre failure mode, the material constant E_{11}, v_{12} and v_{21} is set to zero. Conversely, E_{22}, G_{12} and v_{21} are set to zero in the unidirectional ply of the laminate where matrix failure occurs.

Table 4: Stiffness degradation parameter.

Failure mode	Tensile fibre	Compressive fibre	Tensile matrix	Compressive matrix
Parameter	$E_{11}=E_{22}=G_{12}=v_{12}=v_{21}=0$	$E_{11}=v_{12}=v_{21}=0$	$E_{22}=v_{21}=G_{12}=0$	$E_{22}=v_{12}=v_{21}=G_{12}=0$

In the Hashin failure criterion, three independent damage variables are introduced into the relationships between effective and nominal stresses ($\hat{\sigma}$ and σ):

$$\hat{\sigma}=\begin{bmatrix}\hat{\sigma}_{11}\\ \hat{\sigma}_{22}\\ \hat{\sigma}_{12}\end{bmatrix}=\begin{bmatrix}\frac{1}{1-\omega_{11}} & 0 & 0\\ 0 & \frac{1}{1-\omega_{22}} & 0\\ 0 & 0 & \frac{1}{1-\omega_{12}}\end{bmatrix}\begin{bmatrix}\sigma_{11}\\ \sigma_{22}\\ \sigma_{12}\end{bmatrix} \tag{10}$$

where, ω_{11} is the damage variable representing the damage in the fibre direction; ω_{22}describes the damage perpendicular to the fibre direction; and ω_{12} describes the in plane shear failure. ω_{11} and ω_{22} are damage parameters for tension and compression, respectively. In contrast to ω_{11} and ω_{22}, the damage parameter for shear ω_{12} is independent of the sign of the shear stress. The constitutive tensor C is a function of the damage parameter:

$$C_{(\omega)} = \frac{1}{D}\begin{pmatrix} (1-\omega_{11})E_{11} & (1-\omega_{11})(1-\omega_{22})\nu_{21}E_{22} & 0 \\ (1-\omega_{11})(1-\omega_{22})\nu_{12}E_{11} & (1-\omega_{22})E_{22} & 0 \\ 0 & 0 & D(1-\omega_{12})G \end{pmatrix} \quad (11)$$

where

$$D = 1-(1-\omega_{11})(1-\omega_{22})\nu_{12}\nu_{21} \quad (12)$$

For the undamaged material ω_{ij} =0 and for the fully damaged material ω_{ij} =1. The damage evolution is governed by an exponential law:

$$\omega_{ij} = 1-\exp\left[-\frac{1}{m_{ij}e}\left(\frac{\varepsilon}{\varepsilon_{fij}}\right)^{m_{ij}}\right] \quad (13)$$

where, the subscripts *i* and *j* refer to the various combinations of '1' and '2' directions for tensile, compressive and shear stresses; ε_{fij} is the corresponding failure strain; m_{ij} is a Weibull shape parameter and *e* is the Naperian logarithm base.

5. Numerical results

Here, the ability of the various failure criteria described above to predict the experimental impact response seen here are analysed and discussed through the comparison of the experimental and numerical force–displacement curves and failure modes.

5.1. Force-displacement response

Comparisons of experimental and numerically calculated force–displacement responses are given in Fig. 7. Further, the quantitative discrepancies between actual and calculated peak force and corresponding displacement impact responses for each failure criteria, are presented in Table 5 for clarity.

It can be seen that the trends of the experimental force-displacement curves are well approximated by the numerical simulations using the various failure criteria considered. The numerical results do not show the same degree of oscillations observed in the experimental force-displacement curves since the numerical simplification of the impactor as a rigid impactor nose without the associated carriage cannot simulate the vibrations of the sensor mounting plate. In

general, the Chang-Chang failure criterion predicts better the experimental peak forces and corresponding displacements giving mean absolute errors of 9.4% and 4.7%, respectively (Table 5).

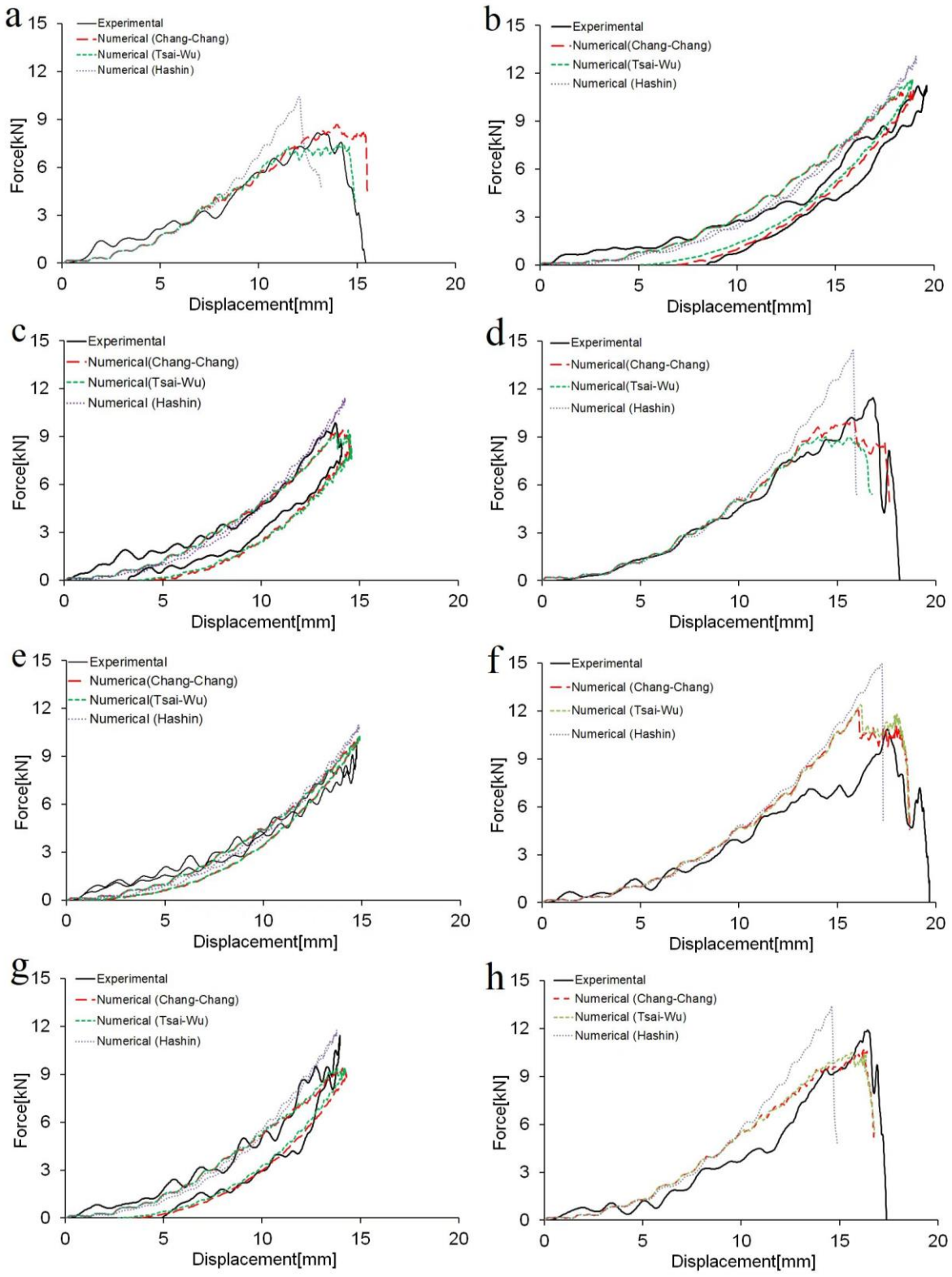

Fig. 7: Comparison of numerical and experimental force-displacement curves. (a): PC-V1.1; (b): PG-V1.2; (c): C1G1-V1.0; (d): C1G1-V1.4; (e): C1G2-V1.0; (f): C1G2-V1.3; (g): C2G1-V1.0; (h): C2G1-V1.2.

Table 5: Comparison of numerical and experimental results.

Specimen	Peak Force (kN)						
	Exp.	Simulation					
		Mat-054	%Error	Mat-055	%Error	Mat-058	%Error
PC-V1.1	8.1	8.7	7%	7.5	-7%	10.4	28%
PG-V1.2	11.2	10.9	-3%	11.6	4%	13.1	17%
C1G1-V1.0	9.9	9.4	-5%	9.4	-5%	11.4	15%
C1G1-V1.4	11.4	10.0	-12%	9.5	-17%	14.5	27%
C1G2-V1.0	9.7	10.2	5%	10.3	6%	11	13%
C1G2-V1.3	10.9	12.1	11%	12.4	14%	15.3	40%
C2G1-V1.0	11.4	9.4	-18%	9.4	-18%	11.8	4%
C2G1-V1.2	12.5	10.7	-14%	10.5	-16%	13.4	7%
PC-V1.1	8.1	8.7	7%	7.5	-7%	10.4	28%
PG-V1.2	11.2	10.9	-3%	11.6	4%	13.1	17%
Ave. Abs. Error (%)	--	--	9.4%	--	10.8%	--	19.0%
Specimen	**Displacement at peak force (mm)**						
	Exp.	**Simulation**					
		Mat-054	**%Error**	**Mat-055**	**%Error**	**Mat-058**	**%Error**
PC-V1.1	13.0	14.1	8%	14.1	8%	12	-8%
PG-V1.2	19.6	18.7	-5%	18.6	-5%	19.1	-3%
C1G1-V1.0	13.6	14.1	4%	14.1	4%	14.2	4%
C1G1-V1.4	16.8	16	-5%	14	-17%	15.8	-6%
C1G2-V1.0	15.2	14.9	-2%	14.9	-2%	14.9	-2%
C1G2-V1.3	17.9	15.7	-12%	15.7	-12%	17.2	-4%
C2G1-V1.0	13.9	14.2	2%	14.2	2%	13.7	-1%
C2G1-V1.2	16.4	16.4	0%	15.7	-4%	14.6	-11%
PC-V1.1	13.0	14.1	8%	14.1	8%	12	-8%
PG-V1.2	19.6	18.7	-5%	18.6	-5%	19.1	-3%
Ave. Abs. Error (%)	--	--	4.7%	--	6.8%	--	4.9%

5.2. Failure mode

Fig. 8 shows the numerically calculated impact damage for each of the eight composite laminates – impact velocity combinations of the experimental tests, using the Chang-Chang failure criterion. These numerical failure patterns can be compared with their experimental equivalents shown in Fig. 5. Due to the mesh size of the shell elements of 4.0 mm used in the finite element modelling, the numerical deformations can only show low resolution results and not exact details of very localised damage.

Fig. 8(a) shows the predicted crack pattern for specimen PC-V1.1. The elements are split along the edge of the impactor, and a cross-shaped crack is formed on the laminate which is consistent with the corresponding experimental result. The deletion of elements underneath the impactor causes the loss of load-carrying capacity, leading to the drop of reaction force in the force-displacement curve (Fig 7a). In Fig. 8(b), no elements are deleted for specimen PG-V1.2, which is

consistent with the experimental results where the specimen suffers only permanent deformation without perforation.

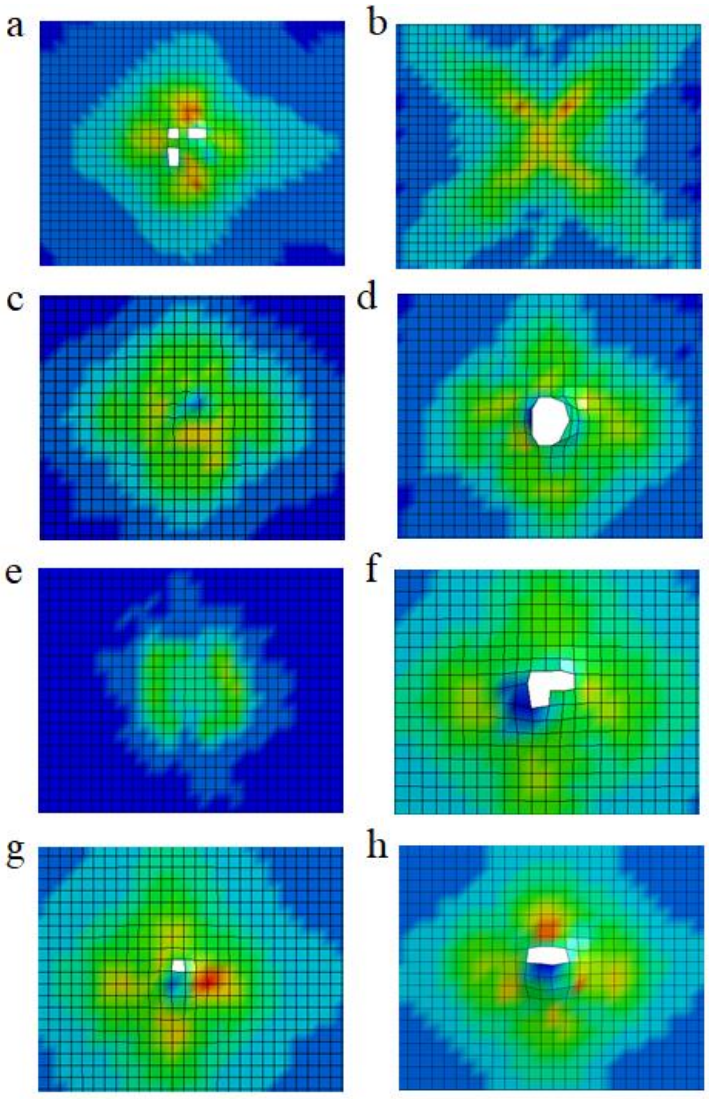

Fig. 8: Failure patterns underneath the impactor. (a): PC-V1.1; (b): PG-V1.2; (c): C1G1-V1.0; (d): C1G1-V1.4; (e): C1G2-V1.0; (f): C1G2-V1.3; (g): C2G1-V1.0; (h): C2G1-V1.2.

For specimens C1G1-V1.0, C1G2-V1.0 and C2G1-V1.0, a higher proportion of carbon fibre content leads to more severe damage (see Fig. 8c, e and g). One finite element is deleted for specimen C2G1-V1.0, predicting the small area of damage underneath the impactor in the experiment (Fig. 5g).

More finite elements are deleted when the impact velocity increases (Figs. 8d, f and h), predicting the more severe damage underneath the impactor in good agreement with the experimental results, demonstrating the suitability of the numerical predictions.

5.3. Relative performances of failure criteria and influence of mesh size

Mesh size can strongly affect numerical results, and thus two more refined mesh sizes, 2 and 5 mm, were then used in the finite element simulations. The three (Chang-Chang, Tsai-Wu and Hashin) failure criteria were again applied.

Here clearer comparisons of the ability of the three numerical models and three mesh sizes to predict the experimental values are made by normalising the numerical results by the experimental results in each case for peak force, displacement and energy at the peak force (Figs. 9-11).

Overall, the Chang-Chang failure criterion gave the most consistently accurate predictions, as compared to the other two failure criteria, for the various mesh sizes considered. Further, the numerical results of all three failure criteria are close to their corresponding experimental displacement and energy at peak force values (Figs.10 and 11)., and the numerical peak forces are reasonably predicted by Chang-Chang and Tsai-Wu (with a maximum error of approximately 20%), whereas the Hashin failure criteria overestimated the peak force compared to the experimental results (Fig. 9).

Generally, the influence of mesh size was only seen to be significantly more influential for the Hashin prediction of peak force, with a finer mesh giving higher accuracy (see Fig. 9). For displacement to peak load, the effect of mesh size is generally not small (Fig. 10), and for energy at peak load the mesh size effect is insignificant, except for a small number of specimen / impact combinations, namely, glass at the lower velocity, and balanced carbon and glass, carbon:glass = 1:2, and carbon:glass = 2:1, all at the higher velocity (Fig. 11).

6. Conclusions

Experimental testing and finite element simulations of laterally impacted carbon-glass hybrid fibre-reinforced polymer composite laminates of varying ratios of carbon to glass have been completed, revealing the various impact deformations and failure mechanisms. Both the impact response and deformation characteristics were predicted with reasonable accuracy by the simulations.

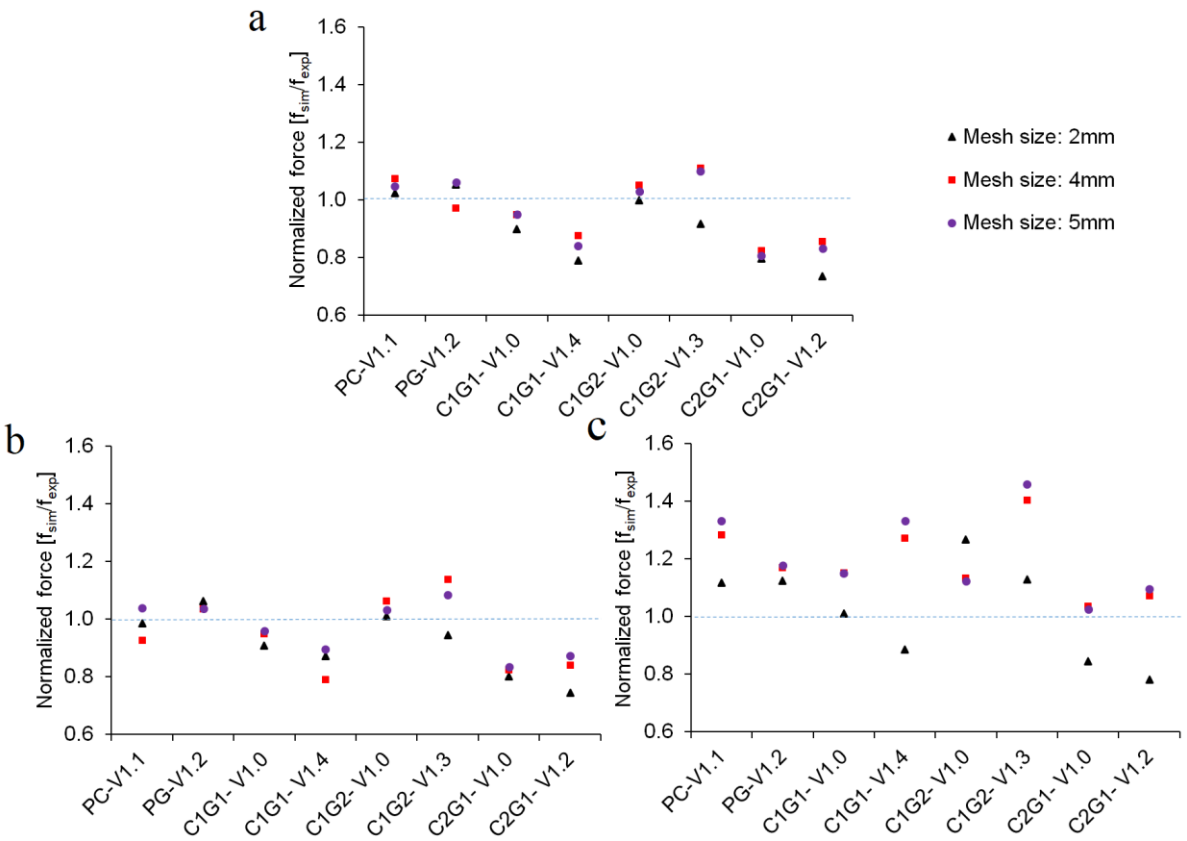

Fig. 9: Ratio between the numerical and experimental peak forces using the (a): Chang-Chang, (b): Tsai-Wu and (c): Hashin failure criterion.

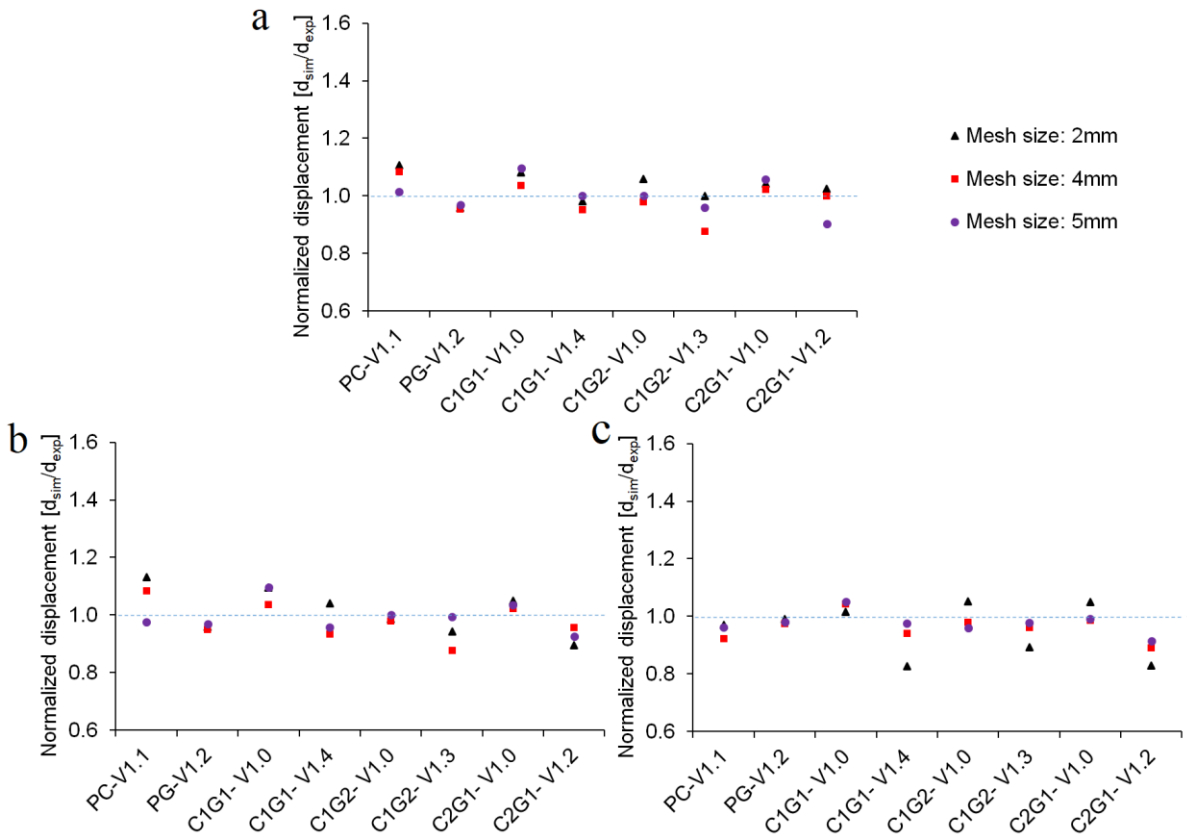

Fig. 10: Ratio between the numerical and experimental displacements at peak force using (a): Chang-Chang, (b): Tsai-Wu and (c): Hashin failure criterion.

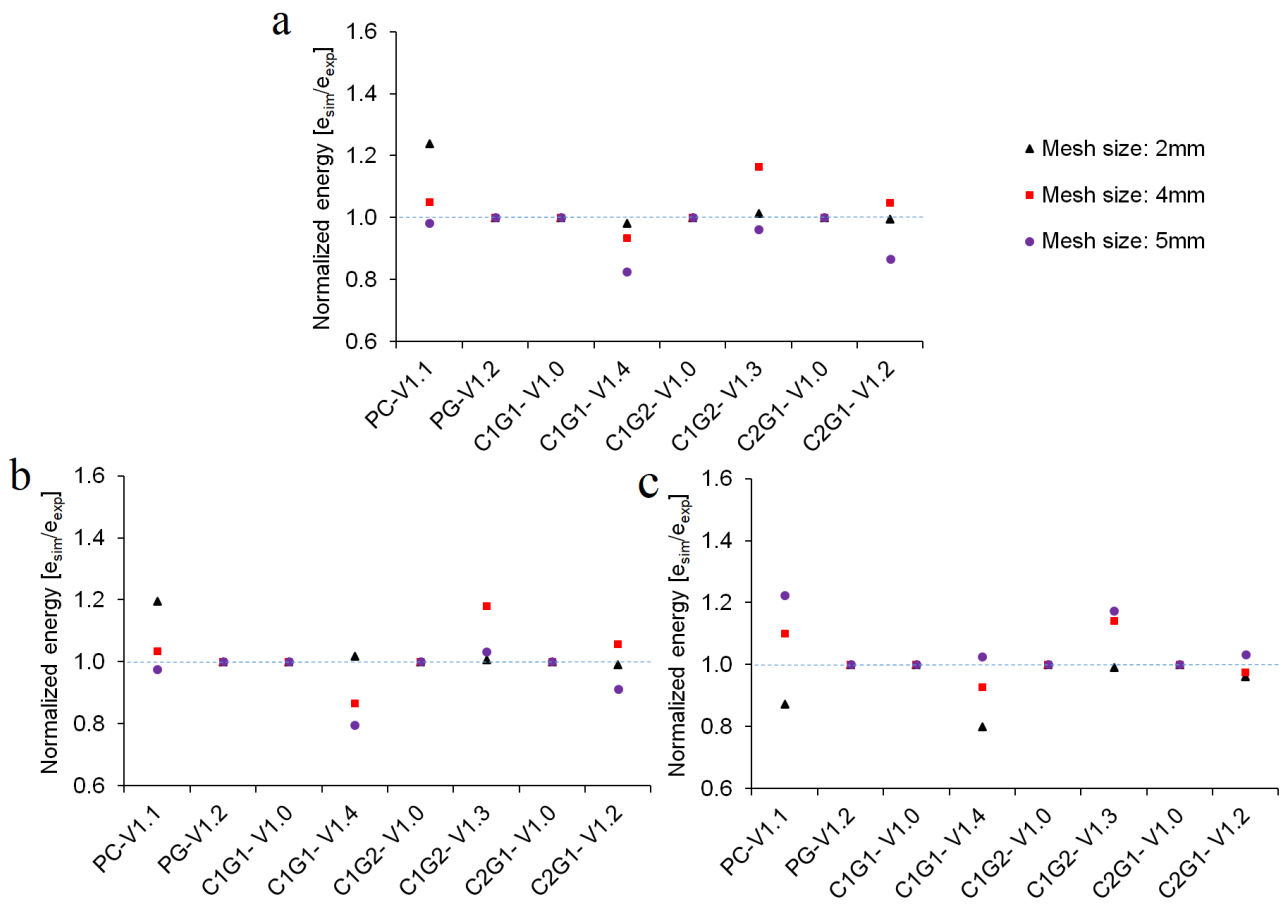

Fig. 11: Ratio between the numerical and experimental energies at peak force using (a): Chang-Chang, (b): Tsai-Wu and (c): Hashin failure criterion.

Carbon fibre has a higher tensile and shear modulus than glass fibre, giving an increased slope force-displacement curve as the ratio of the former fibre is increased. Conversely, the larger elongations of the glass fibre can result in larger deformations, and hence higher impact resistance, of composite laminates containing more of this fibre. In terms of a 'hybrid effect', these advantages of higher carbon fibre moduli and glass fibre elongation can be combined to result in an improved impact response.

For the numerical analyses, the Chang-Chang failure criterion gives the slightly more accurate predictions when compared to those of Tsai-Wu and Hashin, for the materials and impact event considered here. Prediction of peak force was the impact parameter most sensitive here to the choice of mesh size and failure criterion.

CRediT authorship contribution statement

Bin Liu: Methodology, Supervision, Writing - review & editing. **Wei Wang:** Methodology, Formal analysis, Writing - original draft. **Leigh Sutherland:** Supervision, Writing - review & editing.

Declaration of competing interest

The authors declare that they have no known competing financial interests or personal relationships that could have appeared to influence the work reported in this paper.

Acknowledgements

The work is supported by "National Natural Science Foundation of China (Grant No. 52271326)" and "Hainan Provincial Natural Science Foundation of China (Grant No. 623MS069)". L.S. Sutherland was funded by the Portuguese FCT (Fundação para a Ciência e Tecnologia), under the Transitional Standard with contract IST-ID/164/2018. This work contributes to the Strategic Research Plan of the Centre for Marine Technology and Ocean Engineering (CENTEC), which is financed by the Portuguese Foundation for Science and Technology (Fundação para a Ciência e Tecnologia—FCT) under contract UIDB/UIDP/00134/2020.

References

[1] Sutherland LS. A review of impact testing on marine composite materials: Part I – Marine impacts on marine composites. Composite Structures. 2018; 188: 197-208.

[2] Sutherland LS. A review of impact testing on marine composite materials: Part II – Impact event and material parameters. Composite Structures. 2018; 188: 503-511.

[3] Sutherland LS. A review of impact testing on marine composite materials: Part III - Damage tolerance and durability. Composite Structures. 2018; 188: 512-518.

[4] Sutherland LS. A review of impact testing on marine composite materials: Part IV – Scaling, strain rate and marine-type laminates. Composite Structures. 2018; 200: 929-938.

[5] Liu B, Pedersen PT, Zhu L, Zhang S. Review of experiments and calculation procedures for ship collision and grounding damage. Marine Structures 2018; 59: 105-121.

[6] Liu B, Guedes Soares C. Recent developments in ship collision analysis and challenges to an accidental limit state design method. Ocean Engineering. 2023; 270: 113636.

[7] Sharma S, Sudhakara P, Nijjar S, Saini S, Singh G. Recent progress of composite materials in various novel engineering applications. Materials Today: Proceedings 2018; 5(14, Part 2): 28195-28202.

[8] Zhang X, Zhou R, Chen J, Lü Y, Cao D. Influence of low-velocity impact on damage behavior of carbon fiber-reinforced composites. Journal of Wuhan University of Technology-Mater. Sci. Ed 2020; 35(3): 482-487.

[9] Chen D, Yan R, Lu X. Mechanical properties analysis of the naval ship similar model with an integrated sandwich composite superstructure. Ocean Engineering 2021; 232: 109101.

[10] Cantwell WJ, Morton J. The impact resistance of composite materials — a review. Composites. 1991; 22: 347-362.

[11] Jang BZ, Chen LC, Wang CZ, Lin HT, Zee RH. Impact resistance and energy absorption mechanisms in hybrid composites. Composites Science and Technology 1989; 34(4): 305-335.

[12] Pavier MJ, Clarke MP. Experimental techniques for the investigation of the effects of impact damage on carbon-fibre composites. Composites Science and Technology 1995; 55(2): 157-169.

[13] Hosur MV, Adbullah M, Jeelani S. Studies on the low-velocity impact response of woven hybrid composites. Composite Structures 2005; 67(3): 253-262.

[14] Sayer M, Bektaş NB, Sayman O. An experimental investigation on the impact behavior of hybrid composite plates. Composite Structures 2010; 92(5): 1256-1262.

[15] Onal L, Adanur S. Effect of stacking sequence on the mechanical properties of glass–carbon hybrid composites before and after impact. Journal of Industrial Textiles 2002; 31(4): 255-271.

[16] Nayak S, Nayak RK, Panigrahi I. Improvement of low-velocity impact and abrasive wear resistance of carbon/glass fiber-reinforced polymer hybrid composites. Transactions of the Indian Institute of Metals 2021; 74(9): 2245-2254.

[17] Satkar AR, Mache A, Kulkarni A. Numerical investigation on perforation resistance of glass-carbon/epoxy hybrid composite laminate under ballistic impact. Materials Today: Proceedings 2022; 59: 734-741.

[18] Jawaid M, Thariq M, Saba N. Failure Analysis in Biocomposites, Fibre-Reinforced Composites and Hybrid Composites. UK: Woodhead Publishing; 2019.

[19] Tsai SW, Wu EM. A general theory of strength for anisotropic materials. Journal of Composite Materials 1971; 5(1): 58-80.

[20] Hashin Z, Rotem A. A fatigue failure criterion for fiber reinforced materials. Journal of Composite Materials 1973; 7(4): 448-464.

[21] Chang F-K, Chang K-Y. A progressive damage model for laminated composites containing stress concentrations. Journal of Composite Materials 1987; 21(9): 834-855.

[22] Puck A, Schürmann H. Failure analysis of FRP laminates by means of physically based phenomenological models. Composites Science and Technology. 1998; 58: 1045-67.

[23] Hinton MJ, Kaddour AS, Soden PD. Failure Criteria in Fibre-Reinforced-Polymer Composites. Oxford: Elsevier; 2004.

[24] Liu B, Guedes Soares C. Assessment of the strength of double-hull tanker side structures in minor ship collisions. Engineering Structures 2016; 120: 1-12.

[25] Liu B, Villavicencio R, Zhang S, Guedes Soares C. A simple criterion to evaluate the rupture of materials in ship collision simulations. Marine Structures 2017; 54: 92-111.

[26] Cuntze RG. The predictive capability of failure mode concept-based strength criteria for multi-directional laminates—part b. Composites Science and Technology 2004; 64(3): 487-516.

[27] Pinho ST, Iannucci L, Robinson P. Physically-based failure models and criteria for laminated fibre-reinforced composites with emphasis on fibre kinking: Part I: Development. Composites Part A: Applied Science and Manufacturing 2006a; 37(1): 63-73.

[28] Pinho ST, Iannucci L, Robinson P. Physically based failure models and criteria for laminated fibre-reinforced composites with emphasis on fibre kinking. Part II: FE implementation. Composites Part A: Applied Science and Manufacturing 2006b; 37(5): 766-777.

[29] Pinho ST, Darvizeh R, Robinson P, Schuecker C, Camanho PP. Material and structural response of polymer-matrix fibre-reinforced composites. Journal of Composite Materials 2012; 46(19-20): 2313-2341.

[30] Pinho ST, Vyas GM, Robinson P. Material and structural response of polymer-matrix fibre-reinforced composites: Part B. Journal of Composite Materials 2013; 47(6-7): 679-696.

[31] Li N, Gu JF, Chen PH. Fracture plane based failure criteria for fibre-reinforced composites under three-dimensional stress state. Composite Structures 2018; 204: 466-474.

[32] Rezasefat M, Gonzalez-Jimenez A, Giglio M, Manes A. An evaluation of Cuntze and Puck inter fibre failure criteria in simulation of thin CFRP plates subjected to low velocity impact. Composite Structures 2021; 278: 114654.

[33] De Marco Muscat-Fenech C, Cortis J, Cassar C. Impact damage testing on composite marine sandwich panels, part 1: Quasi-static indentation. Journal of Sandwich Structures & Materials. 2014; 16: 341-76.

[34] De Marco Muscat-Fenech C, Cortis J, Cassar C. Impact damage testing on composite marine sandwich panels. Part 2: Instrumented drop weight. Journal of Sandwich Structures & Materials. 2014; 16: 443-80.

[35] Liu B, Villavicencio R, Guedes Soares C. On the failure criterion of aluminum and steel plates subjected to low-velocity impact by a spherical indenter. International Journal of Mechanical Sciences 2014; 80: 1-15.

[36] Liu B, Chen C, Garbatov Y. Material failure criterion in the finite element analysis of aluminium alloy plates under low-velocity impact. Ocean Engineering 2022; 266: 113260.

[37] Marom G, Fischer S, Tuler FR, Wagner HD. Hybrid effects in composites: conditions for positive or negative effects versus rule-of-mixtures behaviour. Journal of Materials Science 1978; 13(7): 1419-1426.

[38] Hallquist JO. LS-DYNA Theory Manual. California, USA: Livermore Software Technology Corporation; 2006.

[39] Liu B, Villavicencio R, Guedes Soares C. Experimental and numerical plastic response and failure of laterally impacted rectangular plates. Journal of Offshore Mechanics and Arctic Engineering 2013; 135(4): 041602

[40] Liu B, Guedes Soares C. Effect of strain rate on dynamic responses of laterally impacted steel plates. International Journal of Mechanical Sciences 2019; 160: 307-317.